Measurements of Planar Target Heating by an Intense Lithium Ion Beam

J.E. Bailey, J.J. MacFarlane, P. Wang, A.L. Carlson, T.A. Haill, D.J. Johnson, P. Lake, E.J. McGuire, T.A. Mehlhorn

May 1997

UWFDM-1046

Submitted to *Physical Review E*.

FUSION TECHNOLOGY INSTITUTE

UNIVERSITY OF WISCONSIN

MADISON WISCONSIN

Measurements of Planar Target Heating by an Intense Lithium Ion Beam

J.E. Bailey, J.J. MacFarlane, P. Wang, A.L. Carlson, T.A. Haill, D.J. Johnson, P. Lake, E.J. McGuire, T.A. Mehlhorn

Fusion Technology Institute
University of Wisconsin
1500 Engineering Drive
Madison, WI 53706

http://fti.neep.wisc.edu

May 1997

UWFDM-1046

Submitted to *Physical Review E*.

Measurements of Planar Target Heating by an Intense Lithium Ion Beam

J.E. Bailey[1], J.J. MacFarlane[2], P. Wang[2], A.L. Carlson[1], T.A. Haill[1], D.J. Johnson[1], P. Lake[3], E.J. McGuire[1], and T.A. Mehlhorn[1]

[1]Sandia National Laboratories, Albuquerque, New Mexico, 87185-1187

[2]Fusion Technology Institute, University of Wisconsin, Madison, Wisconsin, 53706

[3]K-Tech Corporation, Albuquerque, N.M., 87110

The heating of a planar multi-layer (CH / Au / Al / CH) foil target by an intense lithium ion beam is measured using time-integrated spectroscopy of Kα X-ray satellite emission from the Al layer. The time-resolved beam irradiance, kinetic energy, and focal spot size are measured using lithium ions Rutherford-scattered from the foil. The approximately 20 nsec fwhm, 10 MeV peak kinetic energy, Li^{+3} ion beam deposits up to about 435 TW/gm in the Al layer. The peak electron temperature reached in the Al layer is estimated to be 38 - 44 eV by comparing the relative emission intensities from the He-like and Li-like Al with collisional-radiative calculations. The experiment is modeled with a set of 1-D radiation hydrodynamic simulations that calculate the target plasma temperature and density using the measured ion beam parameters as input. A detailed treatment of line transport was found to be essential for accurate calculations of the radiation loss from the Al layer. Synthetic spectra generated by post-processing the simulation results with a collisional-radiative code agree reasonably well with the main features of the experimental spectra, although the emission from the Li- and He-like Al charge states was systematically too weak. Increasing the input beam intensity by 25% resulted in excellent agreement. Considering the ± 30% uncertainty in the measured ion beam irradiance, these results suggest reasonably good overall understanding of the target heating and the atomic processes that influence the Kα emission spectrum.

I. INTRODUCTION

Target heating with light ion beams is a promising method[1,2,3] for achieving Inertial Confinement Fusion (ICF). The baseline approach relies on an indirect-drive hohlraum configuration consisting of a gold sphere filled with low-density CH foam, with the actual ICF capsule at the center[4,5] of the sphere. The ions penetrate the gold wall and deposit their energy in the foam, stopping before they impact the capsule. The radiation from the CH plasma is confined by the gold hohlraum wall, providing a symmetrized bath of x-rays that drives the capsule implosion. High-efficiency ICF implosions depend critically on knowledge of the ion range, since ions that are deposited too deeply inside the hohlraum target are likely to imprint asymmetries on the capsule, while if the ion range is shorter than expected, the hohlraum target mass will be larger than desired for maximum yield. A review of the concepts and available measurements of ion stopping in plasmas is given in Reference 6. Most of the ion stopping is provided by collisions of projectile ions with target electrons. Range shortening, along with a corresponding increase in the energy deposited per unit length (dE/dx), occurs as the target is heated. This is because free electrons resulting from target atom ionization contribute more to the stopping than an equal number of bound electrons. This interrelationship between the ion range and the target plasma created by the beam motivates experiments aimed at understanding ion beam heating. In addition, the radiation flux from the ion-beam-heated plasma inside the hohlraum depends on the plasma temperature, density, and composition. For presently-achievable beam intensities the effect of ion impact inner-shell ionization on the radiation emission from the bulk plasma is relatively small compared to thermal electron effects. The crux to understanding the radiation generation is therefore the ability to predict the plasma temperature and density evolution in response to a specified ion beam irradiation. This

paper describes experiments that address a fundamental question for light-ion-driven ICF: If we irradiate a target with a known ion beam, what target temperature will be achieved?

Experimental information on ion-heated targets has been limited by the difficulties encountered in producing high-power ion beams. Previous related experiments have measured ion slowing in a z-pinch[7,8] or laser-produced plasma[9] that is created independent of the ion beam. The first experiments measuring range shortening in an ion-beam-generated plasma were conducted by F. Young et al.[10] using a ~50 TW/gm deuteron beam. Later experiments [11] extended range shortening measurements to a ~200 TW/gm proton beam. However, neither of these experiments included a measurement of the target temperature. Consequently, the calculations of range shortening that were compared with the data relied on radiation hydrodynamic simulations of the plasma temperature and the resulting ionization distribution. The temperature of heavy-ion-beam produced plasmas has been spectroscopically measured[12,13], but the specific deposition was limited to ~0.3 TW/gm and the resulting plasma temperatures were less than about 1 eV. In recent intense proton[14,15,16] and lithium [17] ion beam experiments with specific depositions up to 1600 TW/gm the target temperature was measured, but in all these experiments a simultaneous measurement of the incident beam irradiance was inhibited by the use of target geometries that maximized the resulting temperature, at the expense of limiting diagnostic access.

The unique feature of the present experiments is a simultaneous measurement of the incident beam and the target response. An approximately 1.2 TW/cm^2, 10 MeV, 20 nsec full width at half maximum (fwhm) Li^{+3} ion beam irradiates a CH/Au/Al/CH multi-layer foil target, reaching a peak specific deposition of about 435 TW/gm in the Al layer. The 1.1 μm total target thickness is

much less than the ion range. A suite of diagnostics uses Rutherford-scattered beam ions (primarily from the Au layer) to measure the time-resolved incident beam kinetic energy, irradiance, and focal spot size. The target temperature is measured using time-integrated Kα X-ray satellite emission from the Al layer. The peak electron temperature in the Al layer exceeds 38-44 eV, determined by comparing the relative intensity of satellites arising from the Li- and He-like aluminum charge states with collisional-radiative calculations. This value is estimated to be ~5% lower than the actual peak temperature because the Kα satellite emission diminishes as the ion beam intensity and kinetic energy drop, while the temperature continues to rise as long as the ion beam deposition is larger than the radiative losses. We evaluate our understanding of the target response using 1-dimensional (1-D) radiation-hydrodynamic simulations with the measured beam properties as the simulation input. Detailed atomic energy level modeling within the radiation-hydrodynamic code was used to provide accurate atomic populations and radiation transport. Comparisons of the detailed line-transport model with more traditional multi-group transport calculations showed that for the Al plasma conditions - optically thin continuum but optically thick lines - the multi-group model overestimates the radiation loss by a factor of 2-5. The detailed treatment used here was therefore essential to obtaining accurate results. Synthetic spectra are computed by post-processing the simulation results with a collisional-radiative code that accounts for both the ion-beam-induced inner-shell ionization and excitations and the thermal-plasma processes. The relative emission intensities of the synthetic spectrum Kα satellite features reproduce the experimental values reasonably well, although the synthetic spectra are systematically somewhat under-ionized. Increasing the simulation input beam intensity by 25% gave better agreement, while an increase of 50% resulted in an over-ionized synthetic spectrum. This indicates that present understanding of the beam-target interaction, including models for both ion beam deposi-

tion and radiation generation and transport, is adequate to provide predictive capability for these experiments, given the ± 30% uncertainty in the measured ion beam irradiance. The sensitivity of the Kα spectra to small changes in the ion beam parameters suggests that this technique can be extended to provide more stringent tests of beam target interaction physics in future experiments.

II. ION BEAM MEASUREMENTS

In our experiments an applied-magnetic-field ion diode[18] converts the electrical power pulse from the Particle Beam Fusion Accelerator II (PBFA II) into an intense lithium ion beam. The cylindrically-symmetric diode accelerates a radially-directed singly-ionized lithium beam across a ~2 cm anode-cathode (AK) gap (Figure 1). The AK gap is insulated against electron losses by a 2-3 T magnetic field applied parallel to the cylindrical axis (see Reference 18). After acceleration, the beam enters a gas cell and is ballistically transported ~13 cm to the target located on the cylinder axis. The beam is stripped into the Li^{+3} charge state upon penetration of the 2-μm-thick mylar membrane that separates the AK gap from the 2-Torr-argon gas cell and it remains approximately fully ionized when it impacts the target. The diode is divided into four 64° azimuthal sectors for diagnostic purposes. The beam from one 64° sector irradiates the planar foil target on the diode axis and the beam from the other three sectors is directed into a variety of other off-axis diagnostics to further evaluate the beam properties. The target is placed at a 45° angle with respect to the diode axis. The foil target consists of a CH / Au / Al / CH sandwich, with typical layer thicknesses 0.2 μm / 0.5 μm / 0.2 μm / 0.2 μm, respectively. The lithium beam deposits only about 10% of its energy (at the 10 MeV peak incident kinetic energy) in this relatively-thin foil. The target was

kept thin compared to the ion range in order to minimize gradients and difficulties with beam diagnostic interpretation, at the expense of lower deposited beam energy. The CH layers are intended to retard the hydrodynamic expansion of the Au and Al layers. The Au layer provides the primary beam diagnostic, since about 95% of the total Rutherford-scattered ion signal results from the gold because of it's high atomic number (Z) and density. Note that a high-Z foil is preferred in Rutherford-scattering intense-beam measurements, rather than simply using scattered ions from the Al, because it avoids complications arising from inelastic scattering events that become more probable at lower target Z. The aluminum layer is chosen because its relatively-simple Kα spectrum provides a measure of the target temperature, as described below.

The ion beam incident on the planar foil targets was measured[19] with a time-resolved ion pinhole camera[20], an energy-resolved time-integrated ion pinhole camera[21,22], and a time-resolved magnetic spectrometer[23-25] that also has 1-D spatial imaging capability. The time-resolved ion pinhole camera uses a 2-D array of PIN diodes to record ions Rutherford-scattered from the target and imaged through a 0.7-mm-diameter pinhole (magnification = 2). This diagnostic is considered to be the most accurate measure of irradiance because of the 2-D imaging and the time resolution. The magnetic spectrometer also records Rutherford-scattered ions with a 2-D PIN array, but in this case one dimension is used to measure the beam kinetic energy and the other provides 1-D spatial imaging. Both time-resolved diagnostics are housed within a 1000 kg tungsten shield to reduce the noise induced in the PIN diodes by the hard x-rays generated from electron losses in the diode. The energy-resolved ion pinhole camera uses a nuclear track recording plastic (CR-39) to record Rutherford-scattered ions imaged separately through six pinholes, with different filter thicknesses to provide energy bins. This instrument provides the best spatial information and

quasi-time resolution can be obtained, since the beam kinetic energy falls monotonically during the pulse.

We first use the magnetic spectrometer to determine the time-resolved beam kinetic energy (voltage) as a function of the horizontal position (z direction in Figure 1). The 1-D spatial imaging capability is important because the instantaneous beam kinetic energy varies with horizontal position by up to 10%. This is in addition to the instantaneous kinetic energy spread at any given target position, which is typically small early in the pulse but can rise to $\pm$ 10% late in the pulse. Knowing the beam kinetic energy, we determine the incident particle current density and the focal spot size on the target from the time-resolved ion pinhole camera, correcting for the energy dependence of the Rutherford-scattering cross section and the time-of-flight from the target to the detector.The magnetic spectrometer is also used to determine the incident particle current density (integrated over the vertical spatial dimension), while the energy-resolved pinhole camera mainly provides a cross-check on the primary time-resolved measurements.The measured lithium ion beam properties from PBFA II experiment #5851 are shown in Figure 2. We have emphasized analysis of this experiment since the irradiance was among the highest values yet achieved and high-quality data was obtained on all essential diagnostics. During the first 10 nsec of the pulse the beam is essentially 100% Li^{+1} in the acceleration gap, impacting the target as Li^{+3}. Later, impurities appear in the beam, but they do not focus onto the target because of deflections in the applied magnetic field. For example, F^{+1} ions accelerated to 7 MeV in the AK gap are stripped into the +5-6 charge state as they enter the gas cell and are deflected horizontally (z direction in Figure 1) by about 7-8 mm from the axis before reaching the target plane. The Li^{+3} irradiance shown in Figure 2 is taken near the peak of the approximately-Gaussian beam profile. The focal

spot size measurements reported in Figure 2 correspond to the dimensions of the beam full-width at half-maximum (fwhm) measured perpendicular to the beam propagation direction. The actual beam spot in the foil plane is elongated in the vertical direction (y in Figure 1) because of the 45° target tilt angle.

The Rutherford-scattering diagnostics measure the ion beam properties after the ions travel through the target. Thus, in order to determine the beam properties incident on the surface of the target, the energy lost by the beam ions in the target plasma must be taken into account. This loss depends on the target plasma temperature because of the range shortening effects mentioned above[6]. The temperature dependence of the energy loss in the hot target was taken into account using an iterative procedure. First the beam irradiance was determined using the cold stopping. Then the radiation hydrodynamic code described below was used to calculate the region-averaged target temperature for each material as a function of time. The irradiance was then re-evaluated using the hot target dE/dx energy loss. The correction has two parts. The incident beam kinetic energy is higher because the energy loss in the hot target is higher than in the cold target. The current density is also higher because the Rutherford scattering cross section is lower when the beam kinetic energy is higher. These two corrections combine for a roughly 10-20% effect on the irradiance during the second half of the pulse after the target has heated up. This correction is relatively small, even though the target heating enhances the energy deposition by up to a factor of 4 (Section IV), because the energy lost in the thin foil target is a relatively small fraction of the incident beam energy.

The uncertainty in the incident beam properties is important because ultimately this limits the

severity of the tests we can apply to our understanding of beam target heating. The irradiance data shown in Figure 2 are an average over the magnetic spectrometer and movie camera results. The variation of the two measurements about the average is less than $\pm$ 15% throughout the pulse, but we estimate[23-25] the absolute uncertainty to be approximately $\pm$ 30%. The possibility of errors in the angular dependence of the incident beam is particularly important because of the $\sin^4 \phi$ term in the Rutherford-scattering cross section. This concern is exacerbated if the beam current density is spatially non-uniform within the 53° sector that irradiates the target, since ions that are preferentially accelerated from either the top or bottom of the anode arrive at the target with greater or smaller incident angles, respectively. An array of Faraday cups located in one of the other sectors is used to verify that global non-uniformities are less than $\pm$ 20%. Ultimately, we must rely on such data from other sectors and on calculations, not measurements, of the beam ion trajectories to estimate the range of incident ion angles actually responsible for heating the target. The errors that result from other factors such as the target thickness, the PIN detector dead layer thickness, and the hot target dE/dx correction are each small, but their cumulative effect can be significant. In addition, although impurity ions are deflected from the target center by the magnetic field, it is difficult to measure the actual impurity ion flux reaching the center of the target because filter and target thicknesses chosen to optimize the lithium signal are sufficient to completely stop most impurities before they reach the PIN detectors.Therefore, we cannot rule out the possibility that impurity ions deposit energy in the target center up to the equivalent of approximately 10% of the total lithium beam energy depostion.Thus, it is difficult to reduce the uncertainty in Rutherford scattering ion beam intensity measurements below $\pm$ 30%.

III. TARGET HEATING MEASUREMENTS

The response of the target to the ion beam heating is measured using Al Kα X-ray satellite spectroscopy. Kα satellite transitions appear when inner-shell ionization from the n = 1 (K) shell of an atom is accompanied by simultaneous vacancies in the n = 2 or n = 3 (L or M) shells. The wavelength of the 1s-2p Kα transition is sensitive to these extra vacancies because the screening of the nucleus experienced by the electron making the 1s-2p transition is reduced when there are fewer spectator electrons. Thus, the satellite lines are blue-shifted with respect to the neutral-atom Kα transition, with the amount of the blue-shift increasing as the number of L- or M-shell vacancies increases. The shift induced by a change in the number of L-shell vacancies produces discrete spectral features and is easily observed. Changes in the M-shell vacancies produce smaller wavelength shifts and generally cause a broadening of the observed transition rather than a separation into discrete spectral peaks.

Kα satellites have been observed in several types of experiments. Examples of the various processes that lead to Kα satellites are displayed in Table 1. An energetic heavy projectile incident on a room-temperature target foil can simultaneously create vacancies in the K and L shells, leading to production of Kα satellites when a 2p electron fills the 1s vacancy (Table 1 (A)). This multiple ionization mechanism has been extensively studied in beam-foil spectroscopy experiments[26]. Kα satellites are also observed when an atom embedded in a hot plasma undergoes simultaneous thermal ionization and bombardment with high-energy projectiles. For moderate plasma temperatures (10-100 eV), thermal ionization of medium-Z atoms such as aluminum produces L-shell vacancies. Energetic electrons or ions incident on a such a hot target produce 1s vacancies by inner-

shell impact ionization, leading to emission of Kα satellites as the 1s holes are filled. An example for an Al target atom initially in the C-like charge state is shown in Table 1 (B). After the inner-shell ionization, the Kα transition occurs in the B-like ion. Such processes are responsible for Kα satellites observed in solar and Tokamak spectra[27], they have been used to measure hot electrons in CO_2 laser experiments[28,29], and they were proposed[30] by Nardi and Zinamon as a means to measure the temperature of ion-heated plasmas. This diagnostic method relies on the emission of a characteristic satellite wavelength by each charge state, so that the target plasma charge state distribution can be determined from the relative intensity of the satellites. The plasma temperature can then be inferred from the ionization distribution, provided some information is available for the plasma density. The first experiments[14] exploiting Kα satellites to diagnose an ion-beam-heated target were performed in 1990, although, as noted above, these experiments offered limited capability to test understanding of beam-heated matter because the incident ion beam was not simultaneously measured. A third type of Kα satellite experiment uses thermal ionization in a hot plasma to produce L-shell holes and the satellite transitions are then observed in absorption using an x-ray backlighter. This has the advantage that the calculations used to infer the temperature rely only on the ionization state and excited state distributions and the transition opacities; the inner-shell ionization cross sections and fluorescence yields are not required. The use of this method in laser-produced and x-ray-heated plasma experiments has become widespread[31-35] in recent years and is presently considered to provide a robust (better than $\pm$ 10% accuracy) temperature diagnostic in the 30-80 eV temperature range. These experiments are relevant to the present, ion-beam-produced, Kα satellite measurements because they provide a database that is used to benchmark the complex atomic physics computer codes used to analyze the data.

The ion-induced Kα satellite technique uses inner-shell transitions to determine the charge state distribution that corresponds to the thermal ionization that existed prior to the inner-shell ionization. This is aided by the fact that each Kα feature primarily arises from a single charge state. However, there is not a one-to-one correspondence between the Kα satellite intensity distribution and the charge state distribution. The atomic physics calculations used to interpret the data must account for the term-dependent fluorescence yields, the charge state dependence of the inner-shell ionization cross sections, and resonant self-absorption. In addition, processes exist that cause transitions from different charge states to overlap. Multiple inner-shell ionization is potentially important because of the finite probability that a beam ion creates one or more L-shell holes, in addition to the K-shell hole. The multiple and single ionization cross sections are comparable for ~10 MeV Li^{+3} projectiles incident on Al I-IV ions, but the multiple ionization cross section decreases rapidly as the target ionization increases because the target atom electrons are more tightly bound. Multiple ionization results in a transition that corresponds to one or more charge states above the usual, single-inner-shell-ionization Kα satellite. An example of multiple ionization of an Al target atom initially in the O-like charge state is shown in Table 1 (C). In this example, two extra vacancies in the 2p shell are created in addition to the 1s inner shell vacancy, and the resulting transition occurs in a B-like Al atom. This emission will overlap with the Kα feature from single ionization shown in Table 1 (B) and must therefore be included in the atomic model. Another process leading to overlapping Kα features is transitions in atoms that were initially in an excited state populated by the thermal plasma processes. An example is shown in Table 1 (D). A N-like Al atom with an electron excited into the n=3 shell produces a transition in C-like Al after the inner shell ionization occurs. However, the wavelength of this transition is similar to transitions in B-like Al, since the screening provided by the 3s spectator electron induces only a small wavelength shift.

The slight red shift of the line due to the extra n=3 spectator makes this contribution difficult to distinguish experimentally from transitions in B-like Al, implying that the collisional radiative calculations must account for both the charge state distribution and the excited state distributions within each charge state. These effects - multiple ionization and excited state configurations - are essential to production of Kα emission from atoms initially in He-, Li-, and Be-like charge states. The ground configurations of these ions initially have no electrons in the 2p state and consequently, either thermal excitation, multiple ionization, or simultaneous ion impact ionization and excitation are required to produce Kα satellites. An example for Kα production from Be-like Al is shown in Table 1(E).

The Kα spectra in the present experiments are recorded with an elliptical crystal spectrograph[36] operated in the Johann-focussing mode[37]. This essentially renders source broadening negligible, a crucial consideration since the scale size of the plasma created by the ion beam is ~ 6-10 mm (Figure 2). The elliptical geometry also has the advantage that the detector is isolated from the line-of-sight to the plasma by the structure of the slit placed at the ellipse focus, reducing the debris and scattered X-rays incident on the detector. The debris resulting from the large energy delivered to the diode routinely destroys the X-ray crystals used in these experiments, but the detector survives intact. A 1.0 or 2.0 mm space-resolving slit provides 2 or 4 mm spatial resolution at the target (magnification = 1). The pentaerythritol (PET) crystal was curved[38] to an 49.2 cm focal-length ellipse with eccentricity typically 0.9188 and height parameter 4.1656 cm (as defined in Reference 36). The range covered in first order was 6.4 - 8.66 Å. The spectral resolution was as high as $\lambda / \delta\lambda \sim 1200$, determined by recording Al Kα spectra from a standard x-ray source. Note that the destruction of the x-ray crystals in each experiment prevented calibrations of

all crystals used and the actual spectral resolution in the data shown below may have been somewhat lower. The spectra are recorded on Kodak DEF film, developed for 5 minutes in GBX developer at 68°. The data below are corrected for the film response[39,40] (including the angle of incidence in the Johann geometry), the nominal crystal reflectivity[41], and the light-tight filter transmission.

A typical time-integrated Kα spectrum from a foil heated by the PBFA-II Li ion beam consists of 1s-2p transitions from Mg-like to He-like aluminum (Figure 3). In Figure 3 the features are labeled according to the charge state in which the transition actually occurs, after inner-shell ionization takes place. The emission from a given Kα satellite at any instant in time depends on the number of target atoms in the appropriate configuration, the number and kinetic energy of the incident projectiles, and the relevant atomic rates. The projectile kinetic energy is important because it affects the inner shell ionization cross section. The intensity of each feature in a time-integrated spectrum (Figure 3) depends on a convolution of the time histories of the target charge state and excited state distributions and the beam current density and kinetic energy. This convolution implies that a complete analysis of time-integrated data requires the use of a hydrodynamic calculation, as described below. However, the lower-charge-state transitions generally originate early in the pulse while the temperature is relatively low and, conversely, the higher-charge-state transitions arise late in the pulse when the temperature is near its peak value. Thus, even in the absence of time-resolved data, we can determine the approximate peak temperature by comparing the relative intensities of the features arising from the He- and Li-like charge states with collisional radiative equilibrium (CRE) calculations. These charge states are the highest observed in this experiment and their emission therefore originates when the temperature is approaching its

maximum value. However, the late-time drop in the beam current and kinetic energy (Figure 2) lead to a significant drop in the Kα emission intensities, while the larger stopping power resulting from the kinetic energy decrease implies that each beam ion provides more efficient target heating.The detailed analysis described in Section IV indicates that the actual temperature maximum occurs about 5 nsec after the Kα emission intensity has dropped below the detection limit. The temperature continues to rise because the ion beam deposition remains larger than the net radiation loss during this period, finally reaching a value that is approximately 3% higher than the result obtained from the intensities of the high-charge-state emission.

CRE calculations were performed to: (1) predict the emergent Kα spectra from the Al layer; and (2) investigate the radiative cooling of the Al and provide benchmark results for testing the simplified CRE model used within the radiation-hydrodynamics code.The CRE code[15] computes atomic level populations by solving multilevel statistical equilibrium equations self-consistently with the radiation field and ion beam properties. Given a temperature and density, the code considers the following processes in determining the populations: Li beam ion-impact ionization of K- and L-shell electrons; electron-impact collisional excitation, de-excitation, ionization, and recombination; photoexcitation and photoionization; spontaneous emission, radiative recombination and dielectronic recombination; and Auger ionization. Multiple ionization is modeled using a modified plane wave Born model[42], with corrections for Coulomb deflection, perturbations of the target wavefunctions induced by the projectile, and relativistic effects on the target ion wavefunction. Benchmark calculations performed using this model show good agreement[42] with beam-target interaction data from cold (un-ionized) target experiments.

In the atomic model, a total of approximately 600 energy levels were considered, distributed over all 14 ionization stages of Al. Roughly one-half of these were autoionization levels which have a K-shell vacancy. The autoionization levels are populated by Li beam ion-impact ionization, and depopulated either by a Kα fluorescence or by Auger ionization. A complete collisional coupling model was utilized for the autoionization states, as well as non-autoionization states. Auger rates and fluorescence yields were computed for each of the autoionization states in our model using an intermediate coupling formalism with Hartree-Fock wavefunctions. Energy levels and oscillator strengths were calculated using a configuration interaction model with Hartree-Fock wavefunctions[43]. The line spectrum was treated in intermediate coupling. Relativistic effects were included in the Breit-Pauli Hamiltonian.

The transport of line radiation was computed using a frequency-averaged escape probability model[44,45], while radiation due to the Al continuum self-emission was transported using a multi-angle, multifrequency integral radiative transfer model. Emergent spectra included opacity effects due to bound-bound, bound-free, and free-free processes. Line shapes were modeled using Voigt profiles, with broadening effects due to Doppler, Stark, natural, and Auger broadening included. Test calculations indicate that at times late in the Li ion beam pulse (i.e., when Kα emission from the highest ionization stages appears), photoionization due to Al self-emission produces a small, but non-negligible, increase in the fractional abundances of the highest ionization stages. On the other hand, photoionization due to the Au radiative emission was found to have a negligible effect in the late-time ionization distribution in the Al layer because of the relatively-low Au temperatures (see below).

The reliability of the CRE calculations was verified by benchmarking[46] against published experimental and theoretical results. Comparisons with laser plasma absorption spectra were used to confirm the accuracy of the level energies, level populations, and oscillator strengths for plasma conditions similar to those encountered here. The portions of the code that are unique to ion-beam-induced emission spectroscopy - namely, the fluorescence yields and inner-shell ionization cross sections - have also been tested as extensively as possible. The fluorescence yield calculations agree to within $\pm$ 7% with previous calculations for Al[47] and Ne[48] plasmas. We expect the present calculations to provide the most accurate results, since the previous work used pure LS[47] and pure JJ[48] coupling. The multiple ionization cross sections are calculated[42] in a similar manner to the well-established methods[49-51] used for cold targets. We verified that the CRE calculations accurately reproduce the available measurements. However, we regard the accuracy of the multiple ionization cross sections as unconfirmed, since the experimental cross sections in the literature are mainly limited to neutral atoms with closed L shell configurations, while we are mainly concerned with open L-shell Al ions. In order to evaluate the possible impact of errors in the multiple ionization cross sections, we varied the cross section and examined the difference in the temperature that would be inferred from the He-like Al to Li-like Al satellite intensity ratio. We considered two extreme cases. First, the multiple ionization cross sections were set equal to zero. This resulted in a temperature that was higher by about 10%. Second, the single (K), double (KL), and triple (KLL) ionization cross sections were multiplied by factors of 2, 4, and 8, respectively. Larger factors were used for transitions with increasing number of ionizations because of larger uncertainties in the calculated cross sections. In this case, the temperature inferred was ~10% lower than the nominal value. These uncertainties are not included in the temperature uncertainties reported elsewhere in this paper, since there is no hard evidence that suggests the nominal cal-

culation are inaccurate.

Figure 4 shows calculated Kα satellite spectra for Al plasmas of uniform temperature and density irradiated by a 10 MeV Li beam. The plasmas have a thickness which corresponds to a solid 2000-Å-thick Al foil. An instrumental broadening of $\lambda/\delta\lambda = 1000$ is included in these calculated spectra. The temperatures and densities span a range typical of those expected to produce the He-like and Li-like satellite emission observed in the experiments. The strongest emission for these plasma conditions is predicted to come from the Heα line and the Li-like abc and qr satellites (see Reference 52 and references therein for satellite definitions). There is a clear trend for increased Heα emission relative to the Li-like satellites as the temperature increases and the density decreases. The He intercombination line near 7.806 Å is blended with the Li-like mn and st satellites and is predicted to be relatively weak for these conditions. The Be-like satellites at $\lambda \sim 7.9$ to 8.0 Å are also fairly weak, in spite of Be-like Al having a higher ionization fraction than the Li- and He-like Al. This occurs both because of resonant self-absorption effects[15,30], and because of the low fluorescence yields of the lower ionization stages.

The experimental intensity ratio of the He-like to Li-like emission is $0.31 \pm 20\%$. The uncertainty in this ratio mainly arises from the weakness of the Heα feature compared to the spectrum noise, making a precise determination of the background intensity difficult. The relative intensities are determined by fitting Gaussian peaks to the data using the ROBFIT line-fitting computer code[53]. The peak plasma electron temperature is estimated from CRE calculations of the line ratio as a function of temperature and density. The $8\text{x}10^{19}$ - $8\text{x}10^{20}$ cm^{-3} electron density range used was suggested by the simulation described below. The plasma electron temperature range consistent

with the experimental ratio and in this density range is T_e = 38-44 eV.

IV. BEAM-TARGET INTERACTION

We evaluated our understanding of the ion beam target interaction using radiation-hydrodynamic simulations performed with the BUCKY[54] 1-D Lagrangian computer code. The measured ion beam parameters are used as input to the code and the resulting target temperature and density evolution are calculated. The ion beam stopping model is based on a method developed by Mehlhorn[55]. Simulations performed with the recently-developed model of Wang and Mehlhorn[56] were found to be similar. The particle angle of incidence is taken into account using particle-in-cell calculations[57] of the projectile trajectories that include 2-D diode geometry effects and the initial 45° target angle. Radiation affects the target response because radiative losses are a significant cooling mechanism and beam energy initially absorbed in one layer (e.g., Au) can be redistributed to other regions (e.g., Al) via radiation emission and absorption. The radiation transport is treated using two models. A multi-group (100 groups) multi-angle model is used for the Au bound-bound, bound-free and free-free radiation, as well as for the continuum radiation in the Al and CH zones. The Au opacities in this model are computed using the unresolved-transition-array model EOSOPA[46], and a detailed configuration accounting model is used for the lower-Z elements. The second model treats the line radiation for the Al and CH using a CRE model embedded within the hydrodynamics code. The CRE model is similar to the model described above, but it uses fewer levels and an escape probability model to reduce computation time. This model includes resonant self-absorption effects and calculates the self-consistent non-LTE atomic level

populations using 222 Al, 43 C, and 4 H levels. The results of the hydrodynamic simulations are post-processed using the stand-alone CRE code since greater atomic physics detail is required to generate accurate spectra than for computing the populations and charge state distributions needed for the plasma evolution. A time integrated synthetic spectrum for comparison with the data is compiled by summing the computed spectra over time.

In our simulations it was found that the temperature in the Al layer at late times was significantly suppressed due to radiation losses. Because of this, a considerable effort was made to accurately model and benchmark the Al radiation physics within the radiation-hydrodynamics code. Note that a similar treatment of detailed radiation physics has been utilized by others[58,59] for high-temperature laser-produced plasmas. Figure 5 shows a comparison of the net radiative cooling rate for an Al plasma computed using 3 models. The solid curve was computed using our stand-alone CRE model. In this calculation a multiangle, multifrequency model, resolving the line profiles in frequency space and including line overlap, was used to treat the radiative transfer. All bound-bound, bound-free, and free-free processes were included in the opacities and emissivities.To provide an indication of the level of detail included in the atomic physics model, Figure 6 shows the frequency-dependent optical depth computed for an Al plasma at T_e = 35 eV, $n_i = 3 \times 10^{19}$ ions cm^{-3}, and a pre-expansion thickness of 2000 Å. The thermally-excited transitions appearing in Figure 6 dominate the radiation losses, while the non-thermal ion-beam-produced Kα transitions provide plasma diagnostic information. The group of lines from roughly 25-60 eV correspond mainly to $\Delta n = 0$ transitions, for example 2s-2p. The group from 100-250 eV corresponds mainly to $\Delta n = 1$ transitions, for example 2p-3d. Note that many of the strongest lines are optically thick, and are therefore prone to resonant self-absorption effects. The continuum, however, is optically

thin over most of the spectrum.

The dot-dashed curve in Figure 5 corresponds to the Al cooling rates calculated using the CRE/ line transport model embedded in the radiation-hydrodynamics code. In this case, each line was transported using a single frequency-averaged opacity in an escape probability model, but with a similar level of detail in the atomic energy level modeling. Note the good agreement between this model and the stand-alone CRE results. The dashed curve in Figure 5 corresponds to the radiative cooling rates computed using a "multigroup" model, in which line opacities and emissivities are grouped into a relatively small number of frequency bins (100 groups) and transported along with the continuum. Thus, in this model the detailed frequency structure is to a large degree lost, and resonant self-absorption effects are not properly accounted for. Note that the radiative cooling rates computed using this more "traditional"approach to radiative transfer are roughly a factor of 2 to 5 higher than those of the more detailed calculations for these plasma conditions. Because the multigroup opacities were computed using an atomic model with the same level of detail as the stand-alone CRE code, the differences are due entirely to the fact that the multigroup transport algorithm does not adequately treat resonance self-absorption effects. Thus, a detailed treatment of line radiation transfer effects is required in our analysis and, in general, this approach should be considered for any target calculation where optically-thick lines but optically-thin continuum radiation is encountered.

The actual ion beam incident on the target at any instant has an approximately-Gaussian 2-D distribution of intensities. The width of the distribution changes as the focal spot size changes in time (Figure 2). Thus, the Kα spectrum at any instant is a sum of emission from regions that have been

heated by different beam intensity histories and that are experiencing different beam current densities at that instant. In order to approximate this complex situation with 1-D simulations, we divided the target into five different spatial regions ranging from the central, most-intense, part of the beam down to the less-intense beam wings. The central region is an ellipse with 1.08 mm minor and 2.3 mm major radii, chosen such that the average irradiance during the early part of the beam pulse was 97% of the peak irradiance shown in Figure 2. The surrounding regions are successively larger elliptical annuli, corresponding to lower irradiance values as the location is further removed from the most intense part of the beam focal spot. We derived the beam irradiance history incident on each region from the Rutherford scattering data and performed a separate 1-D simulation for each region. We then post-processed the results to obtain a synthetic spectrum from each simulation, and combined the spectra together using weighting appropriate to the areas.

The deposition of beam energy and the re-radiation of that energy within the Au and Al target layers is shown in Figure 7. The results in Figure 7 correspond to the simulation for the central simulation ellipse. The beam specific deposition in the Al peaks at 435 TW/gm, compared to about 150 TW/gm for the Au layer. The peak in the deposited power occurs about 2 nsec later than for the incident power, because as the target is heated, the value of dE/dx increases. At peak incident power (12 nsec) the enhancement of the deposited power over the value expected for room temperature materials is approximately 2.4 and 2.0 for the Al and Au, respectively. At 30 nsec the target temperature is higher and the enhancements are 4.5 and 3.1, respectively. Note that the total power deposited in the Au region is actually higher than for the Al because of the higher Au density. The radiation terms are determined by averaging over all the zones within each layer and dividing by the mass.The Au radiation quickly becomes optically thick for both the lines and the

continuum. The net radiation loss grows correspondingly quickly and is comparable to the ion beam heating after about 15 nsec. Conversely, the Al layer never has appreciable continuum opacity, although the optical depths for some of the lines are large (Figure 6). Consequently, the Al radiation is small compared to the Au. There is a brief period around t = 10 nsec when absorption of Au radiation by the Al is sufficient to provide net radiation heating of the Al. Later, the radiation losses dominate the radiation heating, but the radiation loss doesn't become comparable to the ion beam heating until the end of the pulse.

The evolution of the layer-averaged temperatures, densities, and mean ionization stage ($\overline{Z}$) are shown in Figure 8. The results in this Figure again correspond to the central simulation ellipse. The Au layer initially heats quickly in response to the ion beam heating, reaching a maximum electron temperature of T_e = 27 eV. However, as the radiation losses grow and the region expands, the Au plasma electron temperature drops. The Au region expands by an average factor of about 4000 during the pulse, reaching an ion density of about 1.5 x 10^{19} cm^{-3}. In contrast to the Au, the Al plasma electron temperature grows throughout the pulse. The ion beam heating dominates the combined radiation and hydrodynamic-expansion cooling rates. The peak Al electron temperature reaches T_e = 32 eV, about 16-27% lower than the estimate obtained above using the He- to Li-like ratio. This discrepancy is believed to be mainly because of inaccuracies in the input ion beam intensity and the simulation of the target response to the beam, although other factors probably also contribute (see Section V).

The temporal evolution of the synthetic spectra obtained by post processing the simulation results is shown in Figure 9. As expected, the emission from the lower charge states occurs mainly during

the beginning of the pulse and the higher charge state emission occurs later, after the target temperature has risen substantially. The time-integrated intensity of each Kα feature depends on the elapsed time that the plasma spends in the temperature-density regime that favors production of that feature, as well as the beam intensity and kinetic energy during that time interval. Accurate simulation of the relative time-integrated Kα intensities requires that the evolution of the simulation plasma conditions approximates the actual experimental conditions. Thus, even a time-integrated experimental spectrum provides some capability to test the accuracy of the simulation temporal evolution.

A comparison of the experimental spectrum with the time-integral of the baseline simulation spectra is shown in Figure 10 a and b. The main features of the experiment are reproduced reasonably well, although the He- and Li-like features in the synthetic spectrum are too weak. This clearly results from the discrepancy noted above: the peak temperature attained in the simulation is lower than the value obtained using the experimental line ratio and the CRE code. Consequently, the synthetic spectrum appears somewhat under-ionized. A more quantitative comparison is obtained by integrating over the appropriate synthetic spectrum wavelength interval to determine the intensity of the main Kα features. The intervals used are depicted with arrows in Figure 10. The intensity of the corresponding experimental features is determined by fitting Gaussian peaks to the data using ROBFIT[53]. The comparison is displayed in Figure 11. The experimental and simulation relative intensities are represented by solid and dashed histograms, respectively. The relative intensities have been normalized so that the total intensity equals 1.0. Above each feature is a number that gives the ratio of the simulation to experimental relative intensity. This comparison shows that the emission from the C- through F-like features in the simulation are too

bright by 20-100%. The extra intensity in the F- to Mg-like feature implies that the simulation temperature initially rises too slowly, so that the Al remains in the Ne- through Al-like charge states for too long in comparison to the F-, O-, and N-like charge states. The weak emission from the higher charge states, implying that the peak simulation temperature is too low, is discussed below.

V. DISCUSSION

The agreement between the synthetic and experimental spectra is reasonable considering the approximations that have been made. Three other similar experiments were analyzed with a somewhat-simplified atomic model embedded within the radiation hydrodynamics code. Similar results were obtained in all cases: generally reasonable agreement for the lower charge states and weak emission from the higher charge states. This systematic trend prompted us to consider what effects might be responsible for the discrepancies. For this purpose we divided our procedure into four categories: the ion beam measurements, the BUCKY code that calculates the temperature/ density evolution, the CRE code used to generate synthetic spectra from the BUCKY results, and the recording of the experimental spectrum. The relative intensities in the experimental spectrum are affected by the wavelength dependence of the light tight filter, the geometry dependence of the instrument sensitivity, the crystal reflectivity, and the film response. Although the instrument used in these experiments was uncalibrated, we are relying on well-established previous work and consider it unlikely that uncertainties in the experimental spectrum are responsible for the apparent over-ionization of the synthetic spectra. In addition, the benchmarking described above indicates

that the CRE code can accurately reproduce the main Kα features observed in the experiment and is not responsible for the under-ionized synthetic spectra.The impact of the ± 30% uncertainty in the ion beam intensity and uncertainties in the ion beam deposition and radiation transport within the BUCKY code are essentially inseparable, since a higher plasma temperature would result from higher beam irradiance, larger ion beam stopping power, lower radiation cooling, or some combination of the three. In order to evaluate the possible impact of these effects additional simulations were performed using an enhanced beam current density. The synthetic spectra obtained by boosting the input beam intensity by 25% and 50% are shown in Figures 10c and 10d, respectively. Histograms of the relative emission intensities are shown in Figure 11. The simulation with a beam intensity enhancement of 25% gives the best overall agreement, although the simulation Heα intensity is still only 31% of the experimental value. A possible explanation for the remaining difference is discussed below. The simulation with the 50% enhancement is over-ionized, with emission that is too bright from the He-, Li-, and Be-like charge states. The 25% enhancement of the beam intensity is consistent with the estimated ± 30% uncertainty in the ion beam irradiance. However, as noted above, this agreement could be obtained by enhancing the beam deposition or by decreasing the radiation losses. The present results demonstrate that our understanding of the integrated beam heating, radiation emission and transport, and hydrodynamic expansion is valid within the experimental uncertainties. Improved tests of predictive capability will require reduced experimental uncertainty in the beam intensity.

The stand-alone CRE code has been benchmarked[46] against laser plasma absorption spectra and it adequately reproduces the main characteristics of the Kα spectrum in the present experiment. However, there are some discrepancies that appear to be unique to the ion-excited Kα emission

spectrum. An experimental spectrum recorded with somewhat higher spectral resolution makes these discrepancies especially apparent (Figure 12). The calculations displayed in Figure 10 predict an easily discernible splitting of the B-like feature that is not observed in the experiment. Alternatively, we could say that the synthetic spectrum is missing some intensity near the center of the B-like peak. In addition, the atomic model under-predicts the intensity of the feature that appears at 7.77 Å in the experimental spectrum, approximately 13 mÅ to the long wavelength side of Heα. This feature appears in two experiments recorded with higher spectral resolution and it has appeared in prior higher-temperature laser-produced spectra[52,60]. It has been tentatively identified as 1s-2p transition with a 3s spectator electron. This transition is included in the CRE model, but the excited state population is inadequate to explain the experimental intensity. This satellite may be partly responsible for the relatively-high Heα intensity in the Figure 3 spectrum, since in this lower-resolution data the satellite is merged with the resonance line. Based on the Figure 12 spectrum, we estimate that perhaps 30% of the apparent Heα intensity in the lower resolution experimental spectrum (Figure 3) is actually due to this satellite. Subtracting this contribution from the experimental Heα intensity (Figure 10, 11) would considerably improve the agreement obtained with the M = 1.25 synthetic spectrum. Another important discrepancy is the broad quasi-continuum hump under the lower charge state features, indicated with a dotted line in Figures 3 and 12. This quasi continuum does not appear in the synthetic spectra. It is plausible that the quasi continuum hump arises from merging of many weak transitions with a variety of wavelengths. Such emission can result from transitions with n = 3 spectator electrons since the n = 3 spectators induce small wavelength shifts (see Table 1d). As noted above, these transitions are included in the CRE model, but the excited state populations in the model are evidently too low.

The three discrepancies described above (the B-like satellite profile, the satellite 13 mÅ from Heα, and the quasi-continuum hump) all can be explained by a population mechanism missing from the CRE code, although the spitting in the theoretical B-like profile may also be due to inaccuracies in the theoretical wavelengths. One population mechanism that is under investigation is simultaneous ion-beam-induced excitation and ionization events that could lead to 1s-2p inner shell transitions with an n = 3 spectator. Such events are not included at present because a reliable method for calculation of the cross sections is unavailable. Another possibility is that the discrepancies are a reflection of assumptions made in the treatment of ion stopping in plasmas. Although we include the non-thermal processes associated with ion beam-impact ionization in the CRE modeling, we assume that the electron distribution is Maxwellian. The Maxwellian temperature is obtained from the radiation-hydrodynamics calculations, based on the "stopping power" model[55]. In reality, it is possible that the "stopping power" process (ie., ion beam -- target electron collisions) leads to a non-Maxwellian electron distribution in the target. The subsequent interaction of the non-thermal electrons with the atoms in the plasma can then lead to production of Kα satellites with n = 3 spectator electrons. For example, dielectronic recombination is known to populate the levels of interest, but it requires that the energy of the colliding electron be greater than 1.4 keV in order to produce the satellite on the long wavelength side of Heα. Note that these non-thermal processes cannot entirely explain the under-ionization of the synthetic spectrum because the production of the observed He-, Li-, and Be-like intensities would still require higher thermal temperatures than achieved in the radiation-hydrodynamics simulations.

These results represent a significant advance, but further improvements in understanding will require improved experiments. Limitations in the experiment include ± 30% accuracy in the beam

irradiance, averaging of the spectrum over both time and space, and the possible impact of beam non-uniformities. The target temperature has an uncertainty due to the density dependence of the spectra and the lack of an independent density diagnostic. This forces us to rely on the simulations that we are trying to test. The latter problem can be eliminated in future experiments by simultaneously recording spectra from two separate elements with different temperature and density sensitivities (e.g., Al and Mg). In the present experiments the effect of integrating over temporal and spatial gradients is ameliorated by the fact that the spectral emission is directly induced by the ion beam, biasing the emission to reflect the more interesting plasma conditions where the beam intensity is the highest. However, acquisition of time-resolved spectra would clearly provide a more stringent test of our understanding. The extension of Kα spectroscopy to diagnose ion-heated targets using the target self-emission and the demonstration that simultaneous Rutherford-scattering beam diagnostics are compatible with spectroscopic target-heating measurements paves the way for future improved experiments. Using the present results as a guide, we are designing more-ideal experiments using multiple elements, time-resolved x-ray detection, improved beam intensity measurements, and dot-spectroscopy[61] to reduce effects of gradients.

ACKNOWLEDGEMENT

The authors thank the PBFA II operations crew for assistance with the experiments and D.L. Cook, R.J. Leeper, and J.P. Quintenz for continuous support and encouragement. We are grateful to A.B. Filuk for proofreading the manuscript. This work was supported by the United States Department of Energy under contract #DE-AC04-94AL85000. Sandia is a multiprogram laboratory operated by Sandia Corporation, a Lockheed Martin Company, for the United States Department of Energy.

References

1. J.P. VanDevender and D.L. Cook, *Science* **232**, 831 (1986).

2. J. P. Quintenz et al., Proc. 15th Int. Conf. on Plasma Phys. and Contr. Nucl. Fusion Res., IAEA, Seville, 1994, Vol. 3, p. 39 (IAEA - CN-60/B-6).

3. J.P. VanDevender and H. Bluhm, *Nuclear Fusion By Inertial Confinement,* ed. by G. Vellarde, Y. Ronen, and J. M. Martinez-Val, CRC Press, Ann Arbor (1993), p. 455.

4. S.A. Slutz, Private communication (1979), and *Laser and Part. Beams* **13**, 243 (1995).

5. T.A. Mehlhorn et al., *Laser Interaction and Related Plasma Phenomena*, Vol. 10, Plenum Press New York, p. 553 (1992).

6. Z. Zinamon, *Nuclear Fusion By Inertial Confinement* ,ed. by G. Vellarde, Y. Ronen, and J. M. Martinez-Val, CRC Press, Ann Arbor (1993), p. 119.

7. D. H. H. Hoffman et al. *Z. Phys. A* **30**, 339 (1988).

8. D. Gardes et al., *Europhys. Lett.* **8**, 701 (1988).

9. C. Stoekl, private communication (1996).

10. F.C. Young et al., *Phys. Rev. Lett.* **49**, 549 (1982).

11. J.N. Olsen et al., *J. Appl. Phys.* **58**, 2958 (1985).

12. J. Jacoby et al., *Phys. Rev. Lett.* **65**, 2007 (1990).

13. G.E. Belyaev et al., *Laser and Part. Beams* **10**, 737 (1992).

14. J. Bailey et al., *Laser and Part. Beams* **8**, 555 (1990).

15. J.J. MacFarlane et al., *Phys. Rev. E* **47**, 2748 (1993).

16. G.A. Chandler et al., *Rev. Sci. Instrum.* **63**, 4828 (1992).

17. M.S. Derzon et al., *Phys Rev. Lett.* **76**, 435 (1996).

18. D.J. Johnson et al., Proc. 7th IEEE Pulsed Power Conf., Monterey, CA., ed. by R. White and

B.H. Bernstein, p. 944 (1989).

19. R.J. Leeper et al., *Rev. Sci. Instrum.* **59**, 1860 (1988).

20. W.A. Stygar et al., *Rev. Sci. Instrum.* **59**, 1703 (1988).

21. W.A. Stygar et al., *Rev. Sci. Instrum.* **63**, 4860 (1992).

22. L.P. Mix et al., *Rev. Sci. Instrum.* **63**, 4863 (1992).

23. R.J. Leeper et al., in *Proc. NATO Advanced Study Institute on Fast Electrical and Optical Diagnostic Principles and Techniques*, Vol.1, ed. by J.E. Thompson and L.H. Luessen (Martinus Nijhoff, The Netherlands), 1986, pp. 263-359.

24. R.J. Leeper et al., *J. Appl. Phys.* **60**, 4059 (1986).

25. R.J. Leeper et al., in Proc. of 8th Int. Conf. on High Power Part. Beams, ed. by B.N. Breitzman and B.A. Knyazev (World Scientific, NY, 1990), p. 173.

26. J.D. Garcia, R.J. Fortner, and T.M. Kavanagh, *Rev. Mod. Phys.* **45**, 111 (1973).

27. L.L. House, *Astrophys. Jour. Suppl. Ser.* **18**, 21 (1969) and P. Beiersdorfer et al., *Astrophys. Jour.* **409** (#2/pt.1), p. 846 (1993)..

28. J.D. Hares, J.D. Kilkenny, M.H. Key, and J.G. Lunney, *Phys. Rev. Lett.* **42**, 1216 (1979).

29. N.H. Burnett et al., *Phys. Rev. A* **29**, 2294 (1984).

30. E. Nardi and Z. Zinamon, *J. Appl. Phys.* **52**, 7075 (1981).

31. S.J. Davidson et al., *Appl. Phys. Lett.* **52**; 847 (1988).

32. C. Chenais-Popovics et al., *Phys. Rev. A* **40**, 3194 (1989).

33. T.S. Perry et al., *Phys. Rev. Lett.* **67**, 3784 (1991).

34. R.C. Mancini, C.F. Hooper Jr., and R.L. Coldwell, *J. Quant. Spectr. Radiat. Trans* **51**, 201 (1994).

35. T.S. Perry et al., *J. Quant. Spectrosc. Radiat. Transfer* **54**, 317 (1995).

36. B.L. Henke, H.T. Yamada, and T.J. Tanaka, *Rev. Sci. Instrum.* **54**, 1311 (1983).

37. B.A. Hammel, D.W. Phillion, and L.E. Ruggles, *Rev. Sci. Instrum.* **61**, 1920 (1990).

38. X-Ray Optics, Inc., Jacksonville FL 32216

39. B.L. Henke et al., *J. Opt. Soc. Am.* **B 3**, 1540 (1986).

40. P.D. Rockett et al. *Appl. Opt.* **24**, 2536 (1985).

41. B.L. Henke, Private Communication

42. P. Wang, J.J. MacFarlane, and G.A. Moses, *Laser and Part. Beams* **13**, 191 (1995).

43. P. Wang, *Phys. Rev. E* **48**, 3934 (1993).

44. J.P. Apruzese et al., *J. Quant. Spectrosc. Radiat. Transfer* 23, 479 (1980).

45. J.P. Apruzese, *J. Quant. Spectrosc. Radiat. Transfer* 34, 447 (1985).

46. J.J. MacFarlane et al., *Laser and Part. Beams* **13**, 231 (1995).

47. F. Combet Faroux, *Journal de Physique*, Coll. C9, Suppl. 12, Tome 48, 199 (1987).

48. M.H. Chen and B. Crasemann, *Phys. Rev. A* **12**, 959, (1975).

49. J.H. McGuire and P. Richard, *Phys. Rev. A* **8**, 1374 (1973).

50. J.M. Hansteen and O.P. Hosebekk, *Phys. Rev. Lett.* **29**, 1361 (1972).

51. R.L. Watson et al., *J. Phys. B* **16**, 835 (1983).

52. V.A. Boiko, A.Ya. Faenov, and S.A. Pikuz, *J. Quant. Spectrosc. Radiat. Transfer* 19, 11 (1978).

53. R.L. Coldwell and G.J. Bamford, The Theory and Operation of Spectral Analysis Using ROBFIT (AIP, NY, 1991).

54. J. J. MacFarlane, G. A. Moses, and R. R. Peterson, "BUCKY-1 -- A 1-D Radiation-Hydrodynamics Code for Simulating Inertial Confinement Fusion High Energy Density Plasmas," University of Wisconsin Fusion Technology

Institute Report No. UWFDM-984, Madison, WI (1995).

55. T.A. Mehlhorn *J. Appl. Phys.* **52**, 6522 (1981).

56. P. Wang and T.A. Mehlhorn, to be published

57. T.A. Haill, "SOPHIA Users Guide Version 1.5", Internal Report, Sandia National Laboratories, March 24, 1995.

58. J. Davis, K. G. Whitney, and J. P. Apruzese, *J. Quant. Spectrosc. Radiat. Transfer* **20**, 353 (1978).

59. D. Duston and J. Davis, *Phys.Rev.A* **23**, 2602 (1981).

60. O. Renner et al., *Laser and Part. Beams* **12**, 539 (1994).

61. M.J. Herbst et al., *Rev. Sci. Instrum.* **53**, 1418 (1982).

Table Caption

1. Processes leading to Kα satellite transitions. In (a) *l* refers to the number of additional L-shell vacancies. Note that for clarity the examples in b-e refer to specific initial configurations, although in general a distribution of charge states and excited states will exist. For all cases the configuration after ion impact decays when a 2p electron fills the 1s hole.

Figure Captions

1. Schematic diagram of the experiments. The diode is cylindrically-symmetric about the center line CL, but only a 64° azimuthal sector is allowed to irradiate the target on axis. The target lies in the plane formed by the z axis and a line in the xy plane at 45°. Note that for clarity, only the top diagnostic suite is shown; more diagnostics are located below the target.

2. Measured lithium ion beam properties from PBFA II experiment # 5851. The beam irradiance is specified at the peak of the approximately-Gaussian intensity distribution.

3. Al Kα X-ray spectrum from PBFA II experiment #5851. The iso-electronic species designations correspond to the Al charge state primarily responsible for the labeled feature.

4. CRE calculations of Kα emission from a 120-μm-thick Al plasma at T_e = 39-45 eV and n_i = 10^{19} -10^{20} cm^{-3}, exposed to a 10 MeV Li^{+3} ion beam. The observation angle is normal to the target surface. The values on the right hand side of the plot matrix refer to the plasma ion density. The mean charge state ($\bar{Z}$) for each case is shown to enable calculation of the corresponding electron density.

5. Radiative cooling rate for an Al plasma, calculated with three different models. The solid curve is from the stand-alone CRE code and is considered to be the most accurate. The dot-dash curve is from the smaller CRE model embedded within the BUCKY radiation-hydrodynamics code. The dashed curve is from a multi-group radiation transport model which does not adequately treat resonant self-absorption. The pre-expansion plasma thickness in all cases was taken to be 2000 Å.

6. Optical depth of an Al plasma at $T_e = 35$ eV, $n_i = 3 \times 10^{19}$ cm^{-3}, and a pre-expansion thickness of 2000 Å, calculated with the stand-alone CRE model.

7. Power balance calculated with the BUCKY radiation-hydrodynamic code, using the beam parameters shown in Figure 2 as input. The results shown are region averages over the Al and Au zones. The solid curve is the ion beam deposition and the dashed curve is the net radiation loss.

8. Region-averaged electron temperature, electron density, and $\overline{Z}$ calculated with BUCKY computer simulation for the PBFA II #5851 conditions. The solid curves refer to the Au region and the dashed curves refer to the Al.

9. Temporal evolution of the spectral emission calculated by post-processing the simulation results for PBFA II experiment #5851 with the CRE code.

10. Comparison of PBFA II 5851 experimental spectrum (a) with synthetic spectra. M is the multiplier on the measured ion beam irradiance used as input to the simulation. The synthetic spec-

trum in (b) (M = 1.0) corresponds to the nominal measured beam irradiance while the spectra in (c) and (d) used beam irradiance values that were 25% and 50% higher than the measured value, respectively. The charge state primarily responsible for each Kα feature is indicated on the experimental spectrum. The downward arrows at the top of the figure indicate the wavelength intervals used to determine the relative emission intensities shown in Figure 11.

11. Relative emission intensities for the Kα features in the PBFA II 5851 experiment (solid lines) compared to simulation results (dashed lines). M is the simulation beam intensity multiplier as defined for Figure 10. The relative emission intensities are normalized so that the total equals one. The number at the top of each feature is the ratio of the simulation value to the experimental value.

12. Kα spectrum from PBFA II experiment #6347, recorded with higher spectral resolution than in Figure 3.

Table 1:

Example Description	Initial Configuration	Configuration after ion impact
A) Multiple ion impact ionization, cold Al target	$1s^2 2s^2 2p^6 3s^2 3p$ (Al-like)	$1s2s^2 2p^{6-l}\ 3s^2 3p$ (Mg-like)
B) Single ion impact ionization, hot Al target	$1s^2 2s^2 2p^2$ (C-like)	$1s2s^2 2p^2$ (B-like)
C) Multiple ion impact ionization, hot Al target	$1s^2 2s^2 2p^4$ (O-like)	$1s2s^2 2p^2$ (B-like)
D) Single ion impact ionization, hot Al target	$1s^2 2s^2 2p^2 3s$ (N-like)	$1s2s^2 2p^2 3s$ (C-like)
E) Single ion impact ionization, hot Al target	$1s^2 2s2p$ (Be-like)	1s2s2p (Li-like)

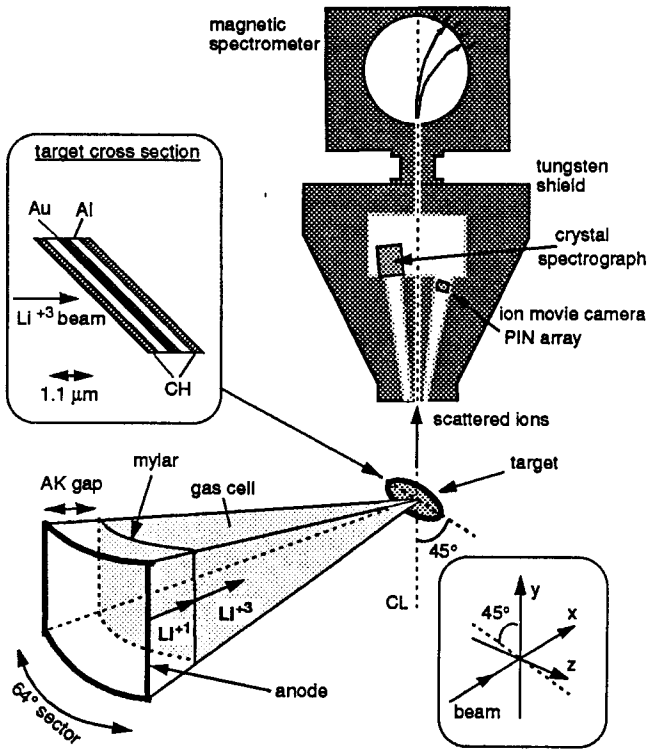

Figure 1

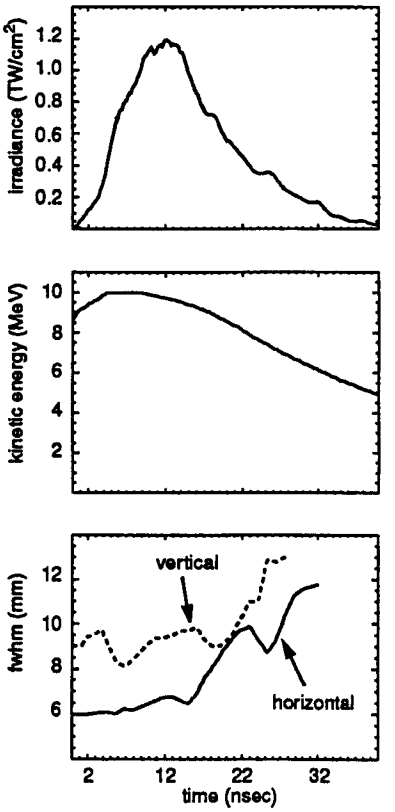

Figure 2

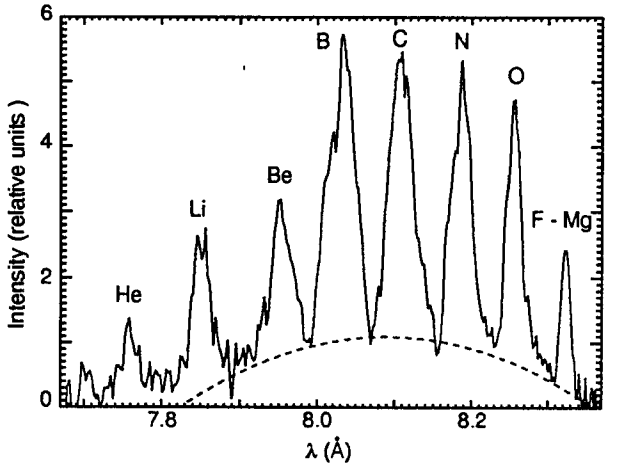

Figure 3

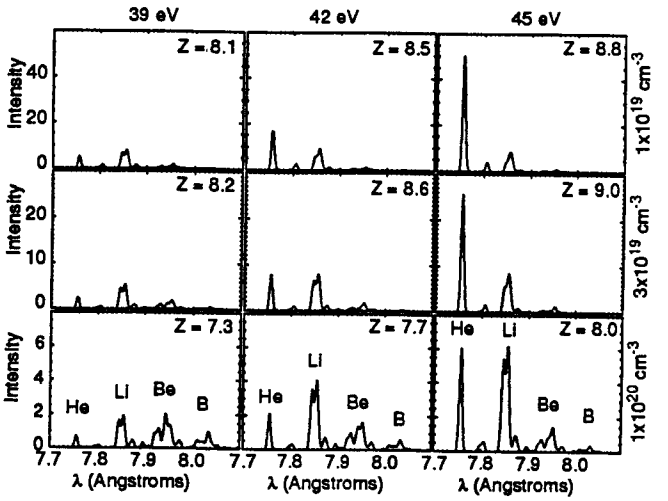

Figure 4

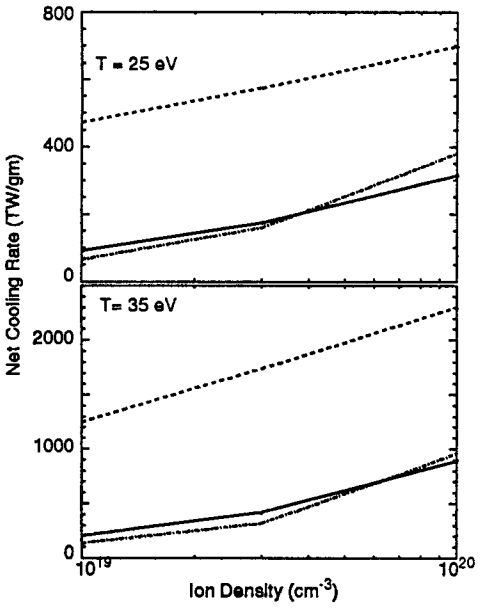

Figure 5

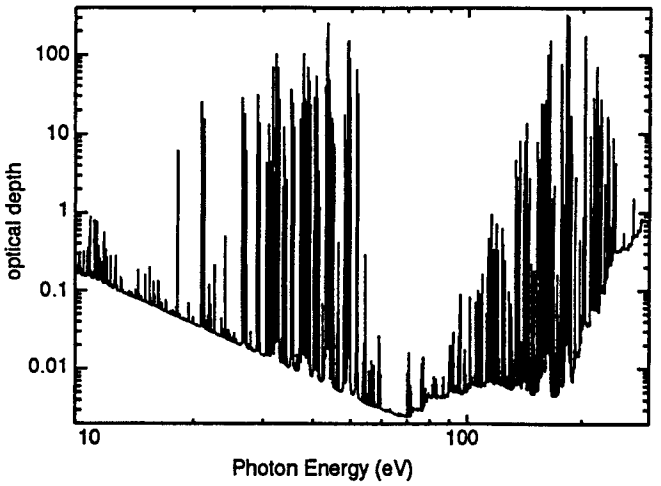

Figure 6

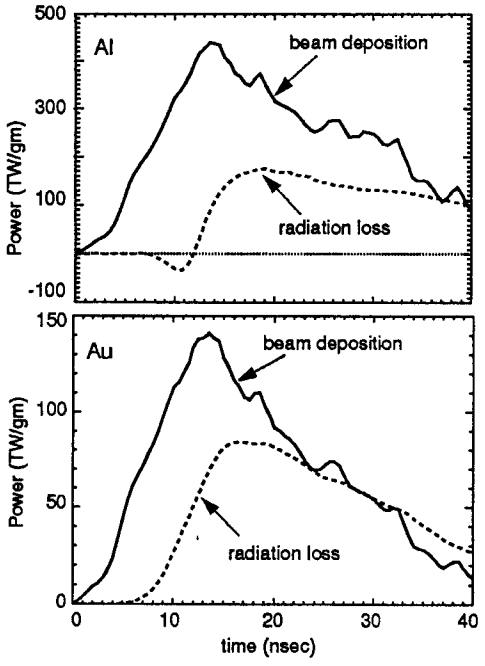

Figure 7

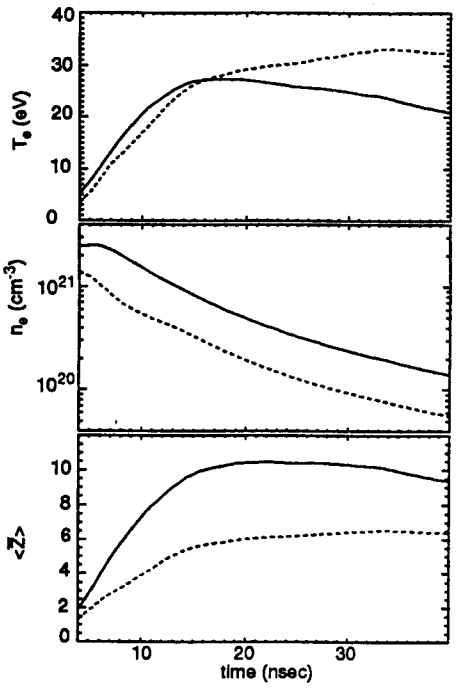

Figure 8

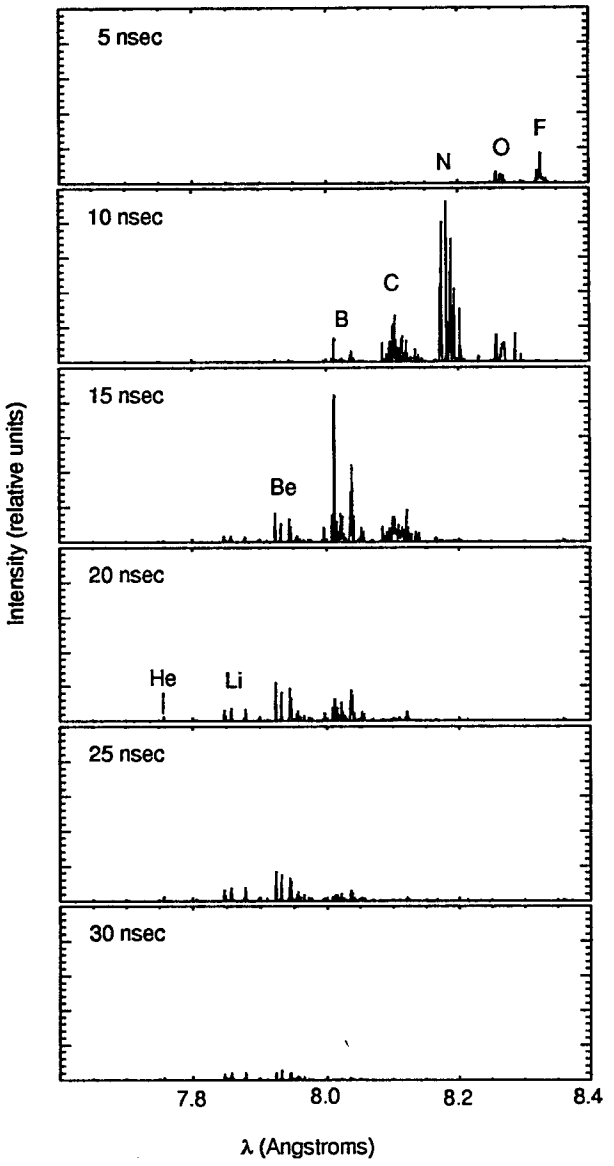

Figure 9

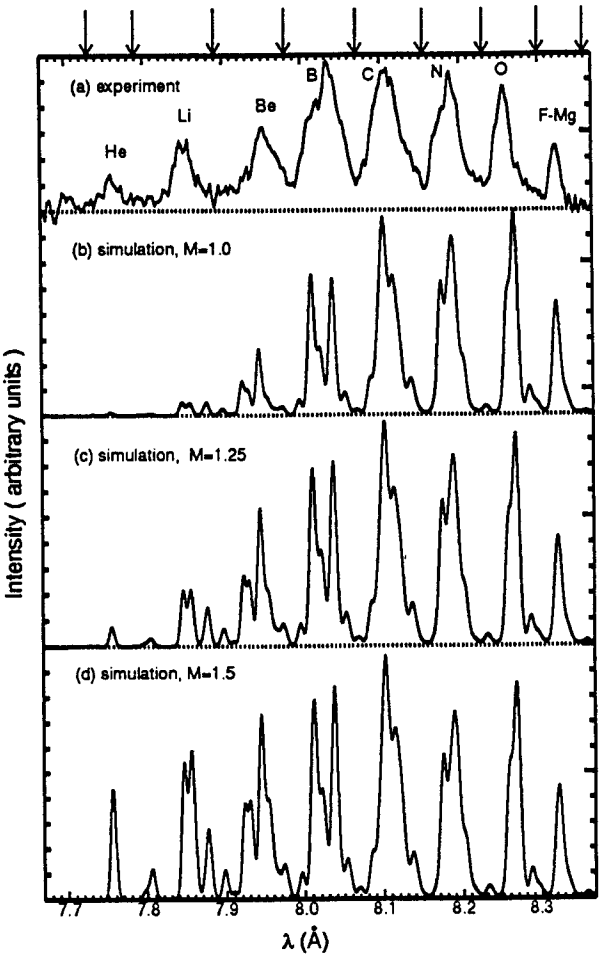

Figure 10

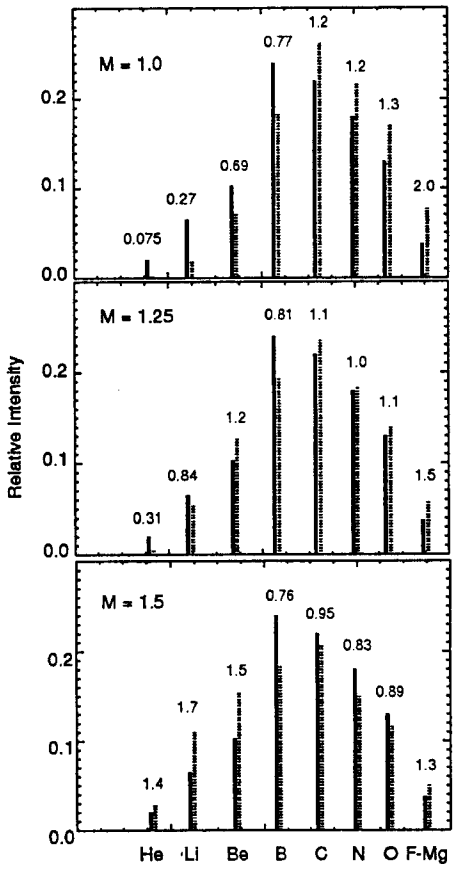

Figure 11

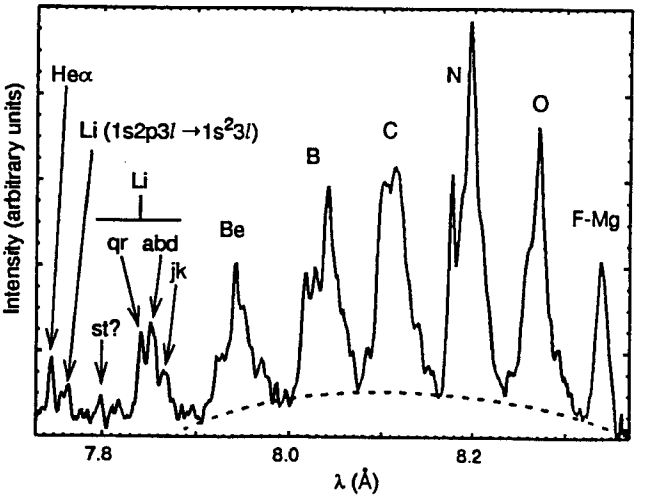

Figure 12